Received: 6 September 2022 | Revised: 24 March 2023 | Accepted: 5 April 2023

DOI: 10.1002/mrm.29680

RESEARCH ARTICLE

Magnetic Resonance in Medicine

Motion-resolved fat-fraction mapping with whole-heart free-running multiecho GRE and pilot tone

Adèle L. C. Mackowiak[1,2,3] | **Christopher W. Roy**[3] | **Jérôme Yerly**[3,4] | **Mariana B. L. Falcão**[3] | **Mario Bacher**[3,5] | **Peter Speier**[5] | **Davide Piccini**[3,6] | **Matthias Stuber**[3,4] | **Jessica A. M. Bastiaansen**[1,2]

[1]Department of Diagnostic, Interventional and Pediatric Radiology (DIPR), Inselspital, Bern University Hospital, University of Bern, Bern, Switzerland

[2]Translation Imaging Center (TIC), Swiss Institute for Translational and Entrepreneurial Medicine, Bern, Switzerland

[3]Department of Radiology, Lausanne University Hospital (CHUV) and University of Lausanne (UNIL), Lausanne, Switzerland

[4]Center for Biomedical Imaging (CIBM), Lausanne, Switzerland

[5]Siemens Healthcare GmbH, Erlangen, Germany

[6]Advanced Clinical Imaging Technology (ACIT), Siemens Healthcare AG, Lausanne, Switzerland

Correspondence
Jessica A. M. Bastiaansen, Laboratory for Quantitative MR Imaging Sciences (QIS LAB), Department of Diagnostic, Interventional and Pediatric Radiology (DIPR), Inselspital, Bern University Hospital, University of Bern, Freiburgstrasse 3, 3010 Bern, Switzerland.
Email: jbastiaansen.mri@gmail.com

Funding information
Emma Muschamp Foundation; Swiss Heart Foundation, Grant/Award Number: FF18054; Swiss National Science Foundation, Grant/Award Numbers: 320030B_201292, 320030_173129, PCEFP2_194296, PZ00P3_167871, PZ00P3_202140

Purpose: To develop a free-running 3D radial whole-heart multiecho gradient echo (ME-GRE) framework for cardiac- and respiratory-motion-resolved fat fraction (FF) quantification.

Methods: ($N_{TE} = 8$) readouts optimized for water–fat separation and quantification were integrated within a continuous non-electrocardiogram-triggered free-breathing 3D radial GRE acquisition. Motion resolution was achieved with pilot tone (PT) navigation, and the extracted cardiac and respiratory signals were compared to those obtained with self-gating (SG). After extra-dimensional golden-angle radial sparse parallel-based image reconstruction, FF, R_2*, and B_0 maps, as well as fat and water images were generated with a maximum-likelihood fitting algorithm. The framework was tested in a fat–water phantom and in 10 healthy volunteers at 1.5 T using $N_{TE} = 4$ and $N_{TE} = 8$ echoes. The separated images and maps were compared with a standard free-breathing electrocardiogram (ECG)-triggered acquisition.

Results: The method was validated in vivo, and physiological motion was resolved over all collected echoes. Across volunteers, PT provided respiratory and cardiac signals in agreement ($r = 0.91$ and $r = 0.72$) with SG of the first echo, and a higher correlation to the ECG (0.1% of missed triggers for PT vs. 5.9% for SG). The framework enabled pericardial fat imaging and quantification throughout the cardiac cycle, revealing a decrease in FF at end-systole by 11.4% ± 3.1% across volunteers ($p < 0.0001$). Motion-resolved end-diastolic 3D FF maps showed good correlation with ECG-triggered measurements (FF bias of −1.06%). A significant difference in free-running FF measured with $N_{TE} = 4$ and $N_{TE} = 8$ was found ($p < 0.0001$ in sub-cutaneous fat and $p < 0.01$ in pericardial fat).

Conclusion: Free-running fat fraction mapping was validated at 1.5 T, enabling ME-GRE-based fat quantification with $N_{TE} = 8$ echoes in 6:15 min.

KEYWORDS
3D radial, cardiac MRI, fat quantification, motion, multiecho GRE, parametric mapping, pilot tone

1 | INTRODUCTION

MRI-derived proton-density fat fraction (PDFF) is considered a robust and reproducible noninvasive measure of fat concentration within the MR research community.[1] Cardiac fat quantification can aid in diagnosing pathologies where adipose cells abnormally develop, within fat depots in dilated cardiomyopathy[2] or within scar tissue of the infracted myocardium leading to an increased risk of arrhythmogenic right ventricular cardiopathy[3,4] and sudden cardiac death.[5,6] Fat fraction (FF) quantification also carries potential to characterize the complex metabolic role of adipose tissues in obesity[7,8] and diabetes,[9,10] in which increased amounts of epicardial, pericardial, and peri-coronary fat alter the cardiovascular disease risk profile.[11,12] Nevertheless, cardiac fat quantification with MRI is seldom performed in clinical settings, where invasive biopsies remain the standard measurement.

PDFF can be quantified using multiecho gradient echo (ME-GRE) MRI sequences that acquire images at different echo times.[13] Multiple echoes are needed to reliably separate the signals in the presence of B_0 field inhomogeneities, which confound fat detection.[14] Dedicated algorithms mitigate the effects of B_0,[15–18] T_1,[19,20] T_2*,[21] or noise,[22] and assume a fixed fat spectral model.[23–25] Accurate fat quantification requires a sufficient number of echoes N_{TE} to resolve the multiple resonance peaks of triglycerides, which lengthens the acquisition time and may limit clinical translation. Because of motion, cardiac PDFF quantifications are typically performed during breath-holds and use triggering devices such as electrocardiograms (ECG). Therefore, such measurements are limited in the number of echoes collected, or restricted in terms of organ coverage. Although free-breathing techniques have enabled whole-heart water–fat separation at 1.5T,[26,27] 3T[28,29] and 7T,[30] they still relied on triggered acquisitions with $N_{TE} \leq 4$, and did not focus on quantification. Alternatively, approaches that combine fingerprinting[31–33] or deep learning[34] with ME-GRE have shown promising results for fat quantification with various N_{TE}, but still required breath-holding and ECG-triggering with restricted organ coverage. To improve spectral resolution with an increased number of echoes while maintaining scan efficiency, alternative motion management techniques are needed.

Recent free-running concepts using uninterrupted 3D acquisitions enable whole-heart free-breathing MRI where ECG time stamps help resolve cardiac motion retrospectively.[35] Free-running sequences have a fixed scan time, improve ease-of-use, and applications range from anatomical imaging,[36–38] to coronary angiography,[39,40] T_1 and T_2 mapping,[41–44] and flow measurements.[45] Advances in respiratory motion compensation extended with a compressed sensing (CS) reconstruction enabled cardiac- and respiratory-motion-resolved 5D imaging.[46,47] The addition of pilot tone (PT) technology[48,49] as an alternative to self-gating (SG) for extracting physiological signals[50] allows sequence-independent motion monitoring. This development could be particularly suitable for long or repeated echo readouts, such as ME-GRE scans, which typically have lower SNR.

To address the challenge of limited organ coverage and restrictions on the number of echoes that can be acquired, a 3D ME-GRE free-running approach was developed for FF quantification. The aim of the study was to combine the strength of motion-resolved cardiac MRI and advanced fat–water decomposition techniques to perform multi-peak fitting of 3D whole-heart ME-GRE data, which are resolved for cardiac and respiratory motion, without needing triggering nor breath-holding. The approach combines (1) an extension of the free-running acquisition to multiecho sampling, (2) PT technology, (3) robust CS reconstruction, and (4) a multi-peak fitting routine for fat–water separation and quantification, with 8 echoes. Phantom and healthy volunteer experiments were performed to test whether the proposed free-running FF mapping framework can provide 3D motion-resolved parametric maps of cardiac adipose tissue.

2 | METHODS

Experiments were performed at 1.5 T (MAGNETOM Sola) using a 12-channel body array equipped with an integrated PT generator. Volunteers, $n = 10$ (F = 5 age [21;31] years old, body mass index [BMI] [19.1;24.7]) provided their informed consent and the study was approved by the local Ethics Committee.

2.1 | Data acquisition, reconstruction, and post-processing framework

2.1.1 | Sequence design

A prototype whole-heart 3D radial free-running GRE sequence was modified to incorporate multiple echo readouts for each radial segment using monopolar readout gradients (Figure 1). The phyllotaxis k-space trajectory consists of radial segments grouped into interleaved spirals, which are successively rotated by the golden angle.[51] The first radial segment of each interleaf is oriented along the superior–inferior (SI) direction. The multiecho readout scheme prolongs the time between two subsequent SI segments of the same echo time TE_i ($i = 1, \ldots, N_{TE}$) within the echo train (Table S1). The SI segments are used to perform

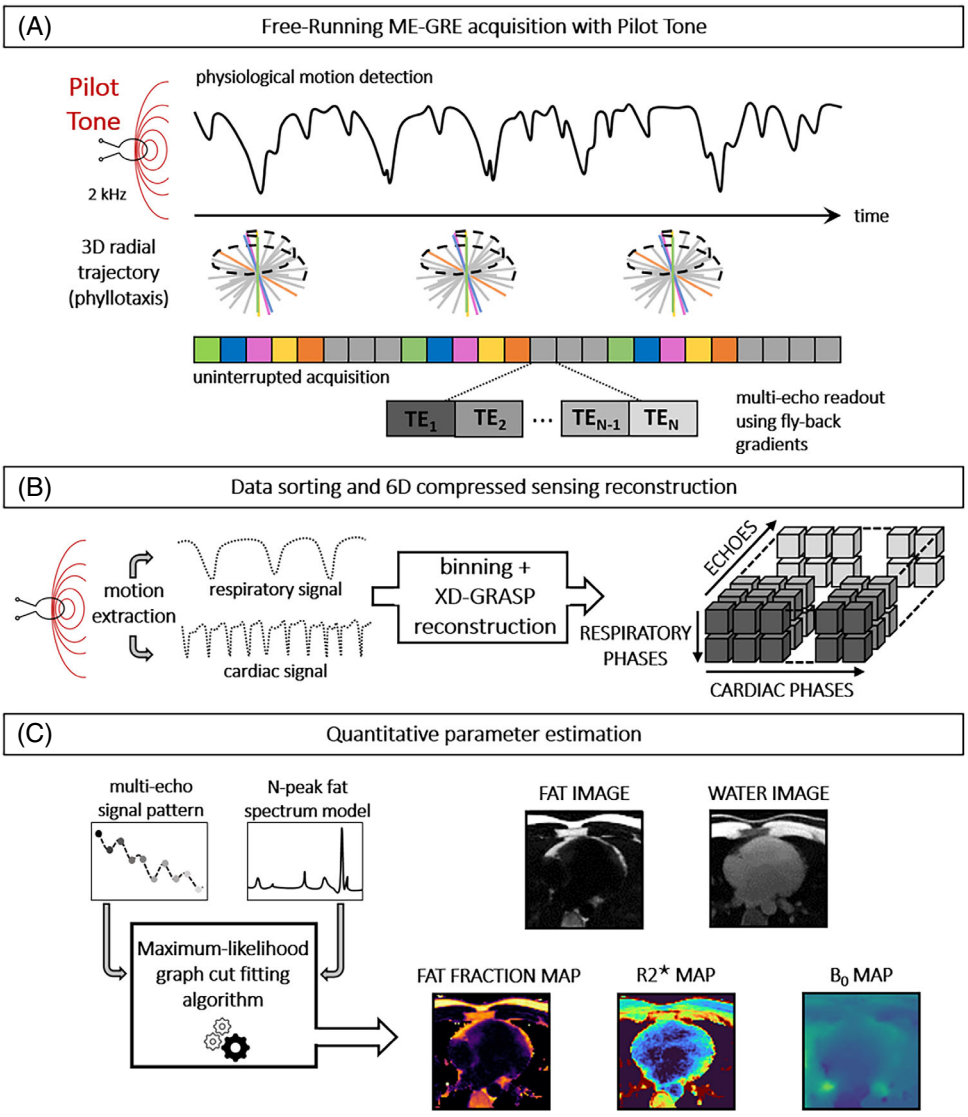

FIGURE 1 Acquisition, reconstruction and post-processing framework. (A) The free-running multiecho gradient echo (GRE) acquisition uses a 3D radial phyllotaxis trajectory, where each k-space line is repeated N_{TE} times with fly-back gradients. During the whole duration of the uninterrupted data acquisition, the coil-integrated pilot tone navigator registers signals at a 2 kHz sampling rate, which are modulated by physiological motion. (B) Acquired signals are used to bin the MR data into cardiac and respiratory motion states. The extra-dimensional golden-angle radial sparse parallel (XD-GRASP) algorithm reconstructs the highly undersampled k-space data into 6D imaging volume. (C) The signal pattern formed along the echo dimension is fed to a fat–water decomposition algorithm, along with a reference fat spectrum, to produce separated fat and water images, as well as fat fraction (FF), water fraction (WF) and main field deviation (B_0) maps.

SG (see Section 2.1.3). The ECG signal was recorded during the scan.

An ECG-triggered version of above sequence was acquired, using the same trajectory, with data collection performed during the diastolic resting phase.

2.1.2 | Acquisition parameters

In vitro

A fat–water phantom with 14 vials containing different fat concentrations (see Figure S1 for details on phantom design[52] and a comparison with a Cartesian acquisition) was scanned using $N_{TE} = 8$ and $N_{TE} = 5$, to mimic, respectively, the free-running and ECG-triggered sequences, and with two RF excitation angles $\alpha = 12°$ and $\alpha = 6°$. Sequence parameters included: a pixel bandwidth of 890 Hz/px, a FOV size of 290 mm^3, an interecho spacing of $\Delta TE = 2.05$ ms, and $TE_1 = 1.25$ ms. The repetition time was TR = 17.02 ms in free-running and TR = 10.87 ms with ECG-triggering.

In vivo

The prototype free-running sequence was designed with a fixed acquisition time (TA) of 6:15 min and isotropic resolution of $(2.0\,mm)^3$ (Table 1). $N_{TE} = 8$ echoes with an interecho spacing $\Delta TE = 2.05$ ms were collected with a trajectory of 22 segments per interleave. The ECG-triggered protocol had a matching FOV, spatial resolution, RF excitation angle, receiver bandwidth, and a similar TA. The ECG-triggered sequence is heart rate-dependent with an average TA = 6:23 min. The time available for echo collection is limited by the cardiac resting phase period. Therefore, the trajectory was set to 12 segments and 437 interleaves in the triggered protocol. This enabled the collection of $N_{TE} = 5$ echoes while producing a similar phyllotaxis pattern as in the free-running protocol (Figure S2), and a slightly higher Nyquist sampling factor (Table 1).

TABLE 1 MR sequence parameters for the free-running and ECG-triggered ME-GRE acquisitions.

MR acquisition	Free-running	ECG-triggered
FOV size [mm^3]	$220 \times 220 \times 220$	$220 \times 220 \times 200$
Spatial resolution [mm^3]	$2.0 \times 2.0 \times 2.0$	$2.0 \times 2.0 \times 2.0$
RF excitation angle [°]	12	12
Receiver bandwidth [Hz/px]	893	893
TR [ms]	17.02	11.04
N_{TE}	8	5
$TE_1/\Delta TE$	1.25/2.05	1.25/2.05
TA [min:s]	6:15	[5:58; 6:64]
$N_{segments} \times N_{interleaves}$	22×1000	12×437
Nyquist sampling factor [%]	5.6	6.4

Note: Sequence parameters were chosen to maximize data collection within a scan time of 6 min, with matching echo times (TE) and inter-echo spacing ΔTE for the free-running and ECG-triggered acquisitions. The Nyquist sampling factor corresponds to the ratio between the k-space lines within one motion bin and the total amount of lines required for a fully sampled reconstruction, expressed in %.
Abbreviations: ECG, electrocardiogram; ME-GRE, multiecho gradient echo.

The proposed free-running sequence induced specific absorption rate (SAR) values ranging from 0.01719 to 0.02197 W/kg in the $n = 10$ volunteers.

2.1.3 | Physiological signals extraction

The coil-integrated PT generator emits a continuous-wave RF signal that is modulated by physiological motion. PT functions at a frequency outside the MR band (62 MHz), therefore, not disturbing image acquisition. The PT data was used to compute 1D respiratory and cardiac signals using principal component analysis (Figure 1), which were then used to divide the raw data into two respiratory and 10 to 11 cardiac motion states. Respiratory motion was addressed by selecting the radial views in the bin corresponding to end-expiration (~40%, as was done previously).[53] Compared to previously published single-echo free-running reconstructions,[39,47,50] the proposed multi-echo framework uses a lower temporal resolution (90 ms per cardiac bin) to guarantee an acceptable undersampling factor (Table 1) for CS reconstruction, as well as sufficient SNR toward the end of the long echo train.

2.1.4 | Motion-resolved image reconstruction

The k-space data were sorted into 6D (x-y-z-cardiac-respiratory-echo) matrices according to the motion states and echo number. The first 220 radial segments were discarded from the reconstruction to eliminate potential transient magnetization effects. The highly undersampled motion-resolved datasets were reconstructed using extra-dimensional golden-angle radial sparse parallel (XD-GRASP)[46,54] and the alternating method of multipliers (ADMM).[55] Regularization using total variation[54] was applied spatially, as well as along two motion-resolved dimensions. No regularization was applied along the echo dimension, so the contrast variations between fat and water remained unaltered. The same regularization, chosen to maintain a good trade-off between visual image quality and motion compression artifacts, was used for all 6D reconstructions (Figure S3).

All 6D reconstructions were performed using MATLAB R2018b (The Mathworks) on a workstation equipped with 2 Intel Xeon CPUs (Intel), 512GB of RAM, and a NVIDIA Tesla GPU (Nvidia). Reconstruction time was recorded using a built-in MATLAB clock.

Respiratory-motion-resolved image reconstruction of the ECG-triggered acquisitions was performed with the same algorithm, with matching regularization where necessary.

2.1.5 | Fat–water separation and quantitative parameters (FF, B_0, R_2*) estimation

The 6D datasets were post-processed to compute fat- and water-only 5D (x-y-z-cardiac-respiratory) images as well as parametric maps (FF, R_2*, B_0) with an iterative graph cut algorithm for fat–water separation,[18,56] part of the ISMRM 2012 Fat/Water Toolbox.[57] The algorithm estimates the B_0 map and computes water and fat fraction maps through fitting a 6-peak spectral fat model with a single T_2* decay component.[23,57] Parameters included: a range of [0;100] Hz for R_2* estimation, a range of [−400;400] Hz for the B_0 map, a number $n = 40$ of graph cut iterations, and a regularization $\lambda = 0.05$. A spatial subsampling with factor $R = 2$ was used to accelerate the B_0 map estimation.

2.2 | Analysis

2.2.1 | Comparison of pilot tone and SG for ME-GRE

Physiological signal extraction using PT was compared to a SG approach. SG uses principal component analysis[58] on the repeated SI projections that encode motion from all active receiver channels. Because eight subsequent SI projections are acquired, the effect of the choice of SI projection for SG of multiecho acquisitions was tested in all

volunteers by performing the SG signal extraction from the eight sets of SI projections (labeled SG TE_i, $i = 1, \ldots, 8$) and comparing it to signals extracted from PT and the reference ECG trace. A Pearson correlation analysis was performed to determine which SG TE_i source provides the closest match to PT and to determine the variability between the different sources. The influence on motion binning was determined by computing a percentage of binning difference to PT. This metric corresponds to the ratio of k-space segments placed into a different bin than the one selected using the PT signal, over the total number of segments. Additionally, a visual comparison was performed on the reconstructed images.

Because SG signals are derived from 3D radial imaging data, they may contain trajectory-made frequency components that are non-physiological and require filtering[47] (Figure S4). To determine the amount of trajectory-dependent information embedded within the SG cardiac signals extracted from each TE, a metric of spectral power removal was used. Spectral power removal corresponds to the percentage of spectral density power removed from the original frequency spectrum after the trajectory-dependent frequency component filtering.[47] This metric informs on the impact of gradient delays and eddy currents on the recorded signal.

Cardiac signals extracted from all sources were also compared to the ECG trace. The mean durations of the cardiac cycle were compared to those measured by the ECG. The number of trigger points throughout the free-running acquisition was reported for the ECG and the other sources, and the percentage of missed triggers (with respect to ECG triggers) was computed. Moreover, the trigger jitter (i.e., the SD of the difference between the time stamps of the ECG triggers and that of each source) was measured. This last metric informs about the accuracy of cardiac cycle length estimation, as the trigger points of each source are not matched with the ECG trigger time; PT triggering is performed on the local minima of the extracted cardiac signal, whereas SG triggering is performed on the zero-crossing point (Figure 4B). Therefore, the trigger jitter measures a deviation across pairs of associated trigger points between the ECG and each evaluated source.

2.2.2 | Parametric mapping analysis

To analyze FF maps, regions of interest (ROIs) were drawn in pericardial fat and sub-cutaneous fat for a static reference. ROIs were drawn based on the visual assessment of the fat-only images. For each tissue type, two ROIs were drawn, both in free-running and in ECG-triggered data. The average FF and SD was computed across cardiac motion states, at expiration. The FF from triggered datasets were compared to those from the diastolic resting phase in the free-running data by linear regression and Bland–Altman analyses.

2.2.3 | Impact of echo train length

To test the impact of N_{TE} on fat quantification, free-running data were undersampled by selecting only the first four echoes (from $TE_1 = 1.25$ ms to $TE_4 = 7.40$ ms). The FF maps obtained with $N_{TE} = 4$ and $N_{TE} = 8$ were compared. The average FF over 10 end-diastolic, expiratory slices in two ROIs in each tissue type was computed. Paired parametric t-tests (GraphPad Prism) were performed in each tissue to determine statistically significant differences.

2.2.4 | Impact of T_1 bias

Because of the shorter T_1 relaxation time of fat compared to water-based tissues, the fat signal measured with GRE imaging is amplified by a factor κ, which depends on the RF excitation angle.[19,22] When defining the true fat fraction as $FF_{true} = F/(W + F)$ where F and W are the respective amplitudes of fat and water signals, the measured fat fraction $FF_{measured}$ deviates from FF_{true} so that $FF_{measured} = \kappa F/(W + \kappa F)$. To evaluate the impact of T_1 bias, numerical simulations of the Bloch equations (MATLAB 2021a, The MathWorks) and phantom experiments were performed. The signal evolution of myocardial and fat tissues was simulated for both the free-running (TR = 17.02 ms) and the ECG-triggered (TR = 11.04 ms) sequences, for a range of RF excitation angles $\alpha \in [1;25]°$. The relaxation times were $T_1 = 996$ ms and $T_2 = 47$ ms for myocardium,[59] and $T_1 = 343$ ms and $T_2 = 58$ ms for sub-cutaneous fat at 1.5 T.[60] For the ECG-triggered sequence, a cardiac cycle length of 900 ms was assumed. The measured fraction $FF_{measured}$ was plotted as a function of FF_{true} for the choice of RF excitation angle $\alpha = 12°$ used in volunteers.

In vitro, the same fat–water separation post-processing was performed as described in volunteer experiments. The FF average and SD was measured in phantom vials across 15 slices and compared to reference values obtained with MRS performed at 9.4T. Following the methodology of Yang et al.,[20] a T_1 bias correction was performed using T_1 estimates ($T_{1fat} = 340$ ms and $T_{1water} = 1350$ ms measured with inversion recovery turbo-spin-echo MRI)[61] on the separated images, and corrected FF values were also calculated and compared with MRS.

In volunteers, T_1 bias correction was performed to adequately compare the free-running and ECG-triggered

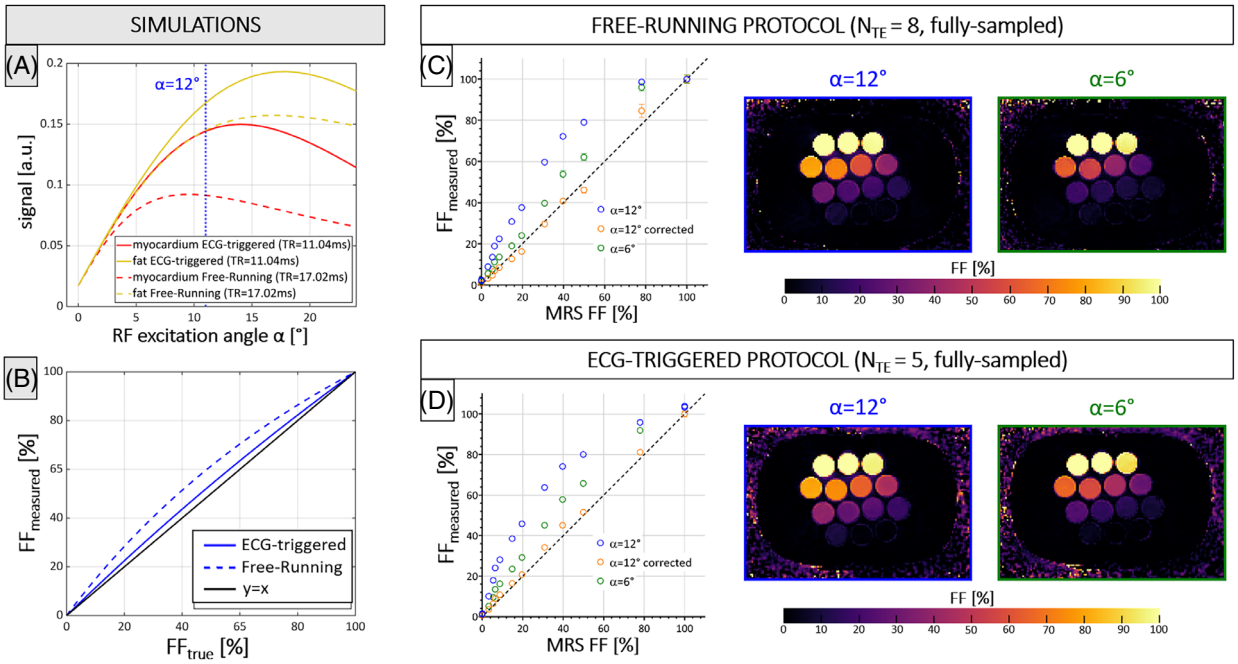

FIGURE 2 Impact of T_1 bias in numerical simulations and in a phantom[52] with controlled fat fractions. Using Bloch simulations, simulated fat and myocardium signals are plotted for different RF excitation angles in a free-running and in an electrocardiogram (ECG)-triggered sequence (A). The blue dotted line indicates the expected signal amplitudes in the current study when using an RF excitation angle $\alpha = 12°$. In (B), the measured fat fraction (FF) obtained with $\alpha = 12°$ is plotted as a function of the true FF, for the free-running and ECG-triggered sequences. In phantom experiments, the average FF measured in maps obtained with free-running (C) and ECG-triggered (D) sequences, with RF excitation angles $\alpha = 12°$ (blue), $\alpha = 6°$ (green), is shown as a function of ground truth FF measured with MRS. T_1 bias-corrected values from the $\alpha = 12°$ protocols are shown in orange on the graphs (C,D). Although the reduced flip angle approach reduced the bias of T_1 to a certain degree, the correction based on T_1 estimates completely eliminated it.

FF maps: for each sequence, the bias estimated from the simulation experiments described above was used.

2.2.5 | Blind scoring

A blind scoring of the water-only and fat-only images and the FF maps with respect to motion resolution, presence of residual sampling artifacts and tissue delineation was performed by two engineers experienced in radial compressed sensing, following a 5-point Likert scale.[62] More information and results can be found in Table S2.

3 | RESULTS

3.1 | Numerical simulations and phantom experiments

3.1.1 | Numerical simulations

A fat signal amplification factor of $\kappa = 1.5854$ was found for an RF excitation angle of 12° (Figure 2A,B, dashed curves). For the ECG-triggered sequence, this factor was $\kappa = 1.1610$ (Figure 2A,B, plain curves). This translated into different correction curves for the free-running and ECG-triggered sequences, where the largest deviation was measured at 11.4% for $FF_{true} = 44.3\%$ with the free-running sequence, and $FF_{true} = 48.1\%$ with a deviation of 3.8% (Figure 2B).

3.1.2 | Phantom experiments

Both the free-running and ECG-triggered protocols demonstrated large deviations because of T_1 bias. Even with a reduced flip angle approach ($\alpha = 6°$) the bias was not completely eliminated (Figure 2C,D). After bias correction with known T_1 estimates, the regression analysis with respect to the MRS controlled FF produced a line described by $y = 1.02x - 0.67$ ($r^2 = 0.995$) for the free-running protocol and $y = 0.99x + 1.73$ ($r^2 = 0.998$) for the ECG-triggered protocol.

3.2 | Motion-resolved multiecho image reconstruction

PT navigation successfully extracted both cardiac and respiratory motion in all 10 healthy volunteers, allowing the

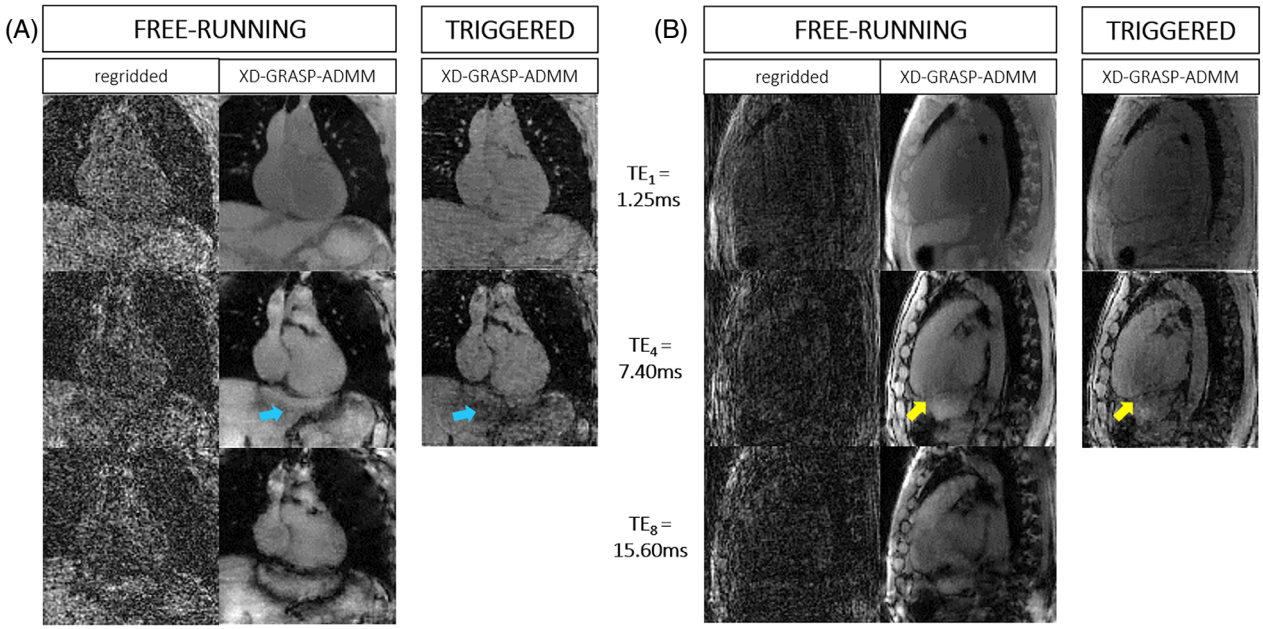

FIGURE 3 Multiecho compressed sensing reconstruction with extra-dimensional golden-angle radial sparse parallel (XD-GRASP)-alternating method of multipliers (ADMM). The effect of XD-GRASP on the different contrast images (at echo times TE_1, TE_4, and TE_8) collected with the pilot tone (PT) free-running multiecho gradient echo (ME-GRE) acquisition is shown in (A) the coronal plane in healthy volunteer V6 and (B) the sagittal plane on healthy volunteer V7. The framework allows recovering of the anatomy absent from the highly undersampled regridded data (5.6% Nyquist), while preserving the contrast change needed for chemical species separation. In comparison, the electrocardiogram (ECG)-triggered 5-echo acquisition (6.4% Nyquist) reconstructed with the same framework displays a slightly higher visual sharpness (B, yellow arrows), but is noisier than the free-running images. The ECG-triggered image at TE_4 shows some signal loss and blurriness in the liver that is less visible in the PT free-running data (A, blue arrows).

echo-specific visualization of motion frames corresponding to the expiration phase of the respiratory cycle, and the end-diastolic phase of the cardiac cycle (Figure 3 and Figure S3). The 10 (11 bins for volunteer V6 who had the longest mean cardiac cycle) cardiac bins had a bin length between [74.5;102.5] ms, with an average bin length of 90.7 ms across volunteers.

The average XD-GRASP reconstruction time for the 10 6D free-running datasets was 5 h 05 min ± 1 h 10 min. For the 10 5D ECG-triggered datasets, the average reconstruction time on the same workstation was 26 ± 4 min.

Free-running images were in visual agreement with reference ECG-triggered images obtained at the diastolic resting phase in terms of anatomy, and showed for each TE anatomical features that cannot be recovered from heavily undersampled data without CS (Figure 3). In addition to signal loss along the echo dimension, additional blurriness at organ interfaces (heart-liver, lung-liver) was also observed at TE_8, compared to TE_1 and TE_4. Despite more data used for each 3D volume reconstructed from the triggered acquisition (6.4% Nyquist against 5.6% for free-running) and the use of the same PT-based respiratory motion correction, signal losses outside the heart were observed in triggered images that were much attenuated in free-running images (Figure 3).

3.3 | Comparison of pilot-tone and SG for ME-GRE

Respiratory signals extracted from the SG sources showed good consistency across echoes, with an average Pearson correlation to PT $r \geq 0.93$ across volunteers (Table 2). As illustrated in volunteer V1, the SG respiratory signals from the first two and the last two recorded echoes showed good agreement with PT, despite a smaller peak-to-peak amplitude reported for PT over the respiratory cycles displayed (Figure 4A). Higher correlation was found across the volunteers for the first two echoes (Table 2). Only the selection of TE_8 as a source tends to increase the deviation from PT binning (18.6% compared to 11% for other sources).

For cardiac motion, variability was observed in the detected cardiac frequency f_{CARD} when a different TE source is used, which is visualized in volunteer V1 over a dozen cardiac cycles in Figure 4B. Overall, the correlation to PT was poorer for cardiac than respiratory signals, with the best correlation at $r = 0.72$ achieved with SG TE_1, and the weakest correlation at $r = 0.36$ with SG TE_7 across volunteers (Table 2). It is worth noting that large SDs were observed across volunteers for this metric.

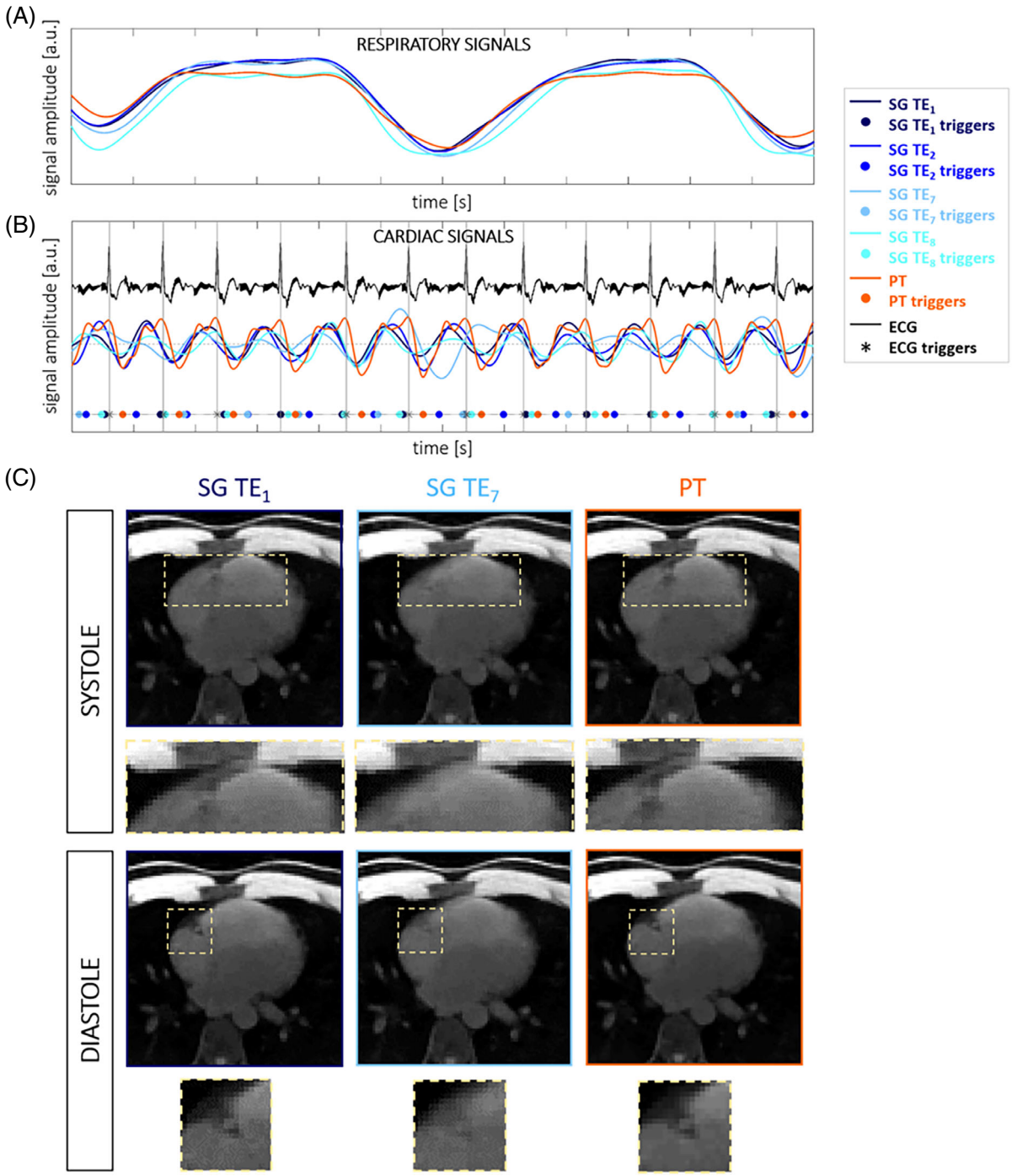

FIGURE 4 Comparison of pilot tone (PT)-based and self-gating (SG)-based physiological signal extraction in V1 and effect on water-only images. (A) Respiratory curves over a 12 s time interval for healthy volunteer V1, obtained from PT data and from the superior–inferior projections of respective echo times TE_1, TE_2, TE_7, and TE_8. (B) Corresponding cardiac signals over the same time interval. Although the SG signals from the first two echoes show good correlation with PT, the signals from SG TE_7 and SG TE_8 present an offset with respect to PT. SG and PT trigger points extracted from each source are shown on the lower line, alongside with the electrocardiogram (ECG) triggers for reference. ECG trigger points correspond to the R-wave, SG trigger points correspond to the zero-crossing (dotted line) of the extracted SG signal, and PT trigger points correspond to the local minima of the extracted PT signal. In V1, a main cardiac frequency $f_{CARD} = 1.03$ Hz was extracted from SG TE_1 and TE_2, whereas $f_{CARD} = 0.75$ Hz was reported with SG TE_7. The reference ECG yielded a mean cardiac cycle length of 1005 ms (Figure S5), corresponding to a main cardiac frequency $f_{CARD} = 1.00$ Hz. (C) Transverse mid-systolic and late-diastolic water-only images obtained from the proposed free-running sequence using the SG signals extracted from TE_1 (left), TE_7 (middle), and using PT signals (right). For both cardiac phases, images from all three physiological signal sources are in good visual agreement. Close-ups of the regions containing the right coronary artery (RCA) show no difference between SG TE_1 and PT, but loss of contrast and additional blur at SG TE_7.

TABLE 2 Comparison of PT-based and SG-based physiological signal extraction parameters in volunteers.

Source	% Spectral power removed	Pearson's *r* correlation to PT, respiratory	Pearson's *r* correlation to PT, cardiac	% Binning difference to PT, respiratory	% Binning difference to PT, cardiac	% Missed ECG triggers	ECG trigger jitter [ms]
SG TE_1	92 ± 5	0.96 ± 0.01	0.72 ± 0.32	12 ± 2	15 ± 4	5.9 ± 4.4	69 ± 22
SG TE_2	60 ± 13	0.96 ± 0.03	0.51 ± 0.24	12 ± 2	14 ± 4	6.8 ± 9.6	87 ± 24
SG TE_3	58 ± 10	0.94 ± 0.06	0.54 ± 0.31	12 ± 2	13 ± 4	9.0 ± 12.8	132 ± 92
SG TE_4	32 ± 11	0.93 ± 0.10	0.66 ± 0.26	11 ± 2	12 ± 4	5.4 ± 8.5	68 ± 22
SG TE_5	30 ± 7	0.92 ± 0.11	0.52 ± 0.32	12 ± 2	13 ± 4	10.8 ± 14.1	65 ± 26
SG TE_6	29 ± 7	0.92 ± 0.11	0.60 ± 0.29	11 ± 1	13 ± 4	6.9 ± 9.5	57 ± 16
SG TE_7	21 ± 9	0.92 ± 0.11	0.36 ± 0.31	11 ± 2	13 ± 4	13.9 ± 14.5	118 ± 102
SG TE_8	28 ± 6	0.91 ± 0.12	0.56 ± 0.30	19 ± 3	13 ± 3	8.5 ± 14.0	85 ± 55
Pilot tone	0	1	1	0	0	0.1 ± 0.1	23 ± 14

Note: The number of SI readouts is repeated by the number of acquired echoes (N_{TE}), which was 8. The cardiac and respiratory signals reconstructed from the 8 different SG and one PT sources are compared by quantification of the following metrics: percentage of spectral power filtered out because of trajectory dependencies (see Figure S4), Pearson correlation coefficient with respect to PT, percentage of difference in binning with respect to PT, percentage of missed trigger points with respect to the reference ECG, and ECG trigger jitter. All reported metrics are given as a mean and standard deviation.
Abbreviations: ECG, electrocardiogram; PT, pilot tone, SG, self-gating, SI, superior–inferior.

The percentage of spectral power removal decreased with increasing source echo time (Table 2). With SG TE_1 as source, an average of 92% of frequency components were identified as trajectory-dependent and therefore, filtered out. However, using the next echo TE_2 as source, this number dropped to 60%. A steady reduction was seen with the use of successive TEs, with the lowest number reported for TE_7. However, no particular trend across echoes was observed in the percentage of binning difference with respect to PT-based binning (Table 2).

The trigger points from the PT cardiac signals had the best match to ECG triggers, with a trigger jitter of (23 ± 14) ms across volunteers and 0.1% of missed triggers. SG TE_7 had the largest deviation from both the PT source and the ECG signal across volunteers, with an average trigger jitter as large as (118 ± 102) ms.

No differences in the chest respiratory positions could be observed, indicating similarity in respiratory signals used for binning. Despite the higher variability in cardiac motion characteristics, the effect on reconstructed images was minor, but visible in the water-only images identified at end-systole and at mid-diastole for SG TE_1, SG TE_7, and PT (Figure 4C). All three sets of images displayed overall good visual agreement and homogenous fat suppression in both the chest and the heart. However, closer inspection of the region containing the right coronary artery (RCA) showed that the images binned based on SG TE_7 signals were blurrier, with a slight loss of contrast in the RCA at diastole.

3.4 | Water–fat separation and parametric mapping

The average post-processing time was 2 h 43 min ± 7 min for free-running and 14 min 37 s ± 18 s for triggered acquisitions.

Water–fat separation with graph cut was successful in all volunteers, without water–fat swaps or motion ghost artifacts. In the maps (Figure 5), no displacement of the expected static (chest, spine) regions was seen, nor ghosting, indicating that respiratory motion compensation was achieved and that cardiac motion compensation did not interfere with organs and tissue in the periphery of the FOV. The displacement of the fatty regions of the heart was clearly observed (Figure 6, animated GIF in Video S1).

Despite the lack of blood-to-myocardium contrast inherent to GRE imaging, the water-only images provided good visualization of cardiac anatomy, with complete absence of fatty tissue, enabling the visualization of the RCA (Figure 5A, top and Figure 6C). In the corresponding fat-only images (Figure 5A, bottom and Figure 6D), 3D visualization of pericardial fat was possible, particularly in coronal orientation around the right atrium and left ventricle. Sub-cutaneous fat-based tissues appeared brighter than cardiac fat tissues; such differences are more apparent in the co-registered quantitative FF and water fraction maps displayed with a color gradient (Figure 5B).

In addition, the proposed framework produced cardiac and respiratory motion-resolved 3D maps of R_2* (Figure 6C, Video S1.c) and B_0 (Figure 6F, Video S1.f).

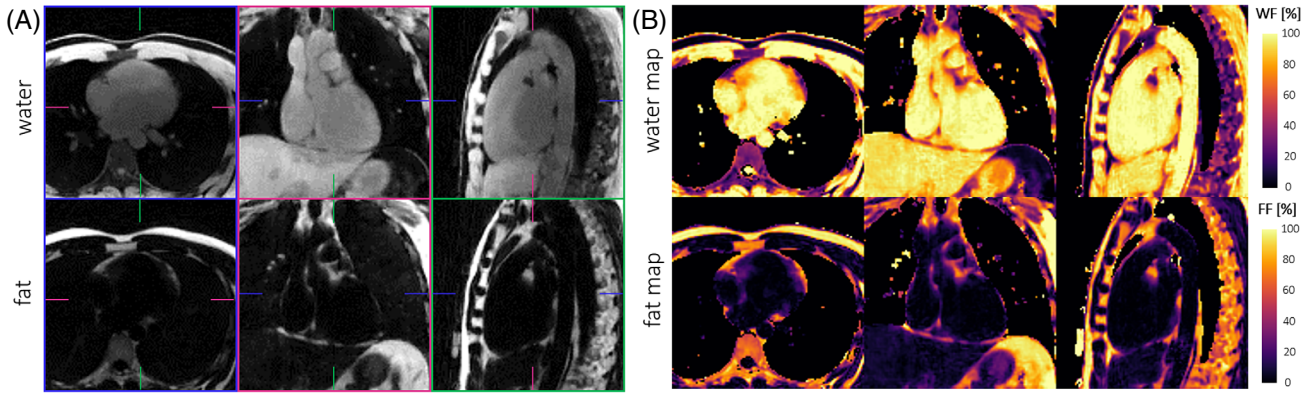

FIGURE 5 Water–fat separation and quantification obtained with the proposed framework. On (A), water-only and fat-only images of healthy volunteer V1 are shown, as obtained after post-processing reconstructed 6D imaging volumes with a maximum-likelihood graph cut fitting algorithm. On (B), the corresponding parametric maps of water fraction and fat fraction are displayed. Slice position with respect to the three traditional MRI views (transversal, coronal, and sagittal) is indicated on (A) by the colored lines.

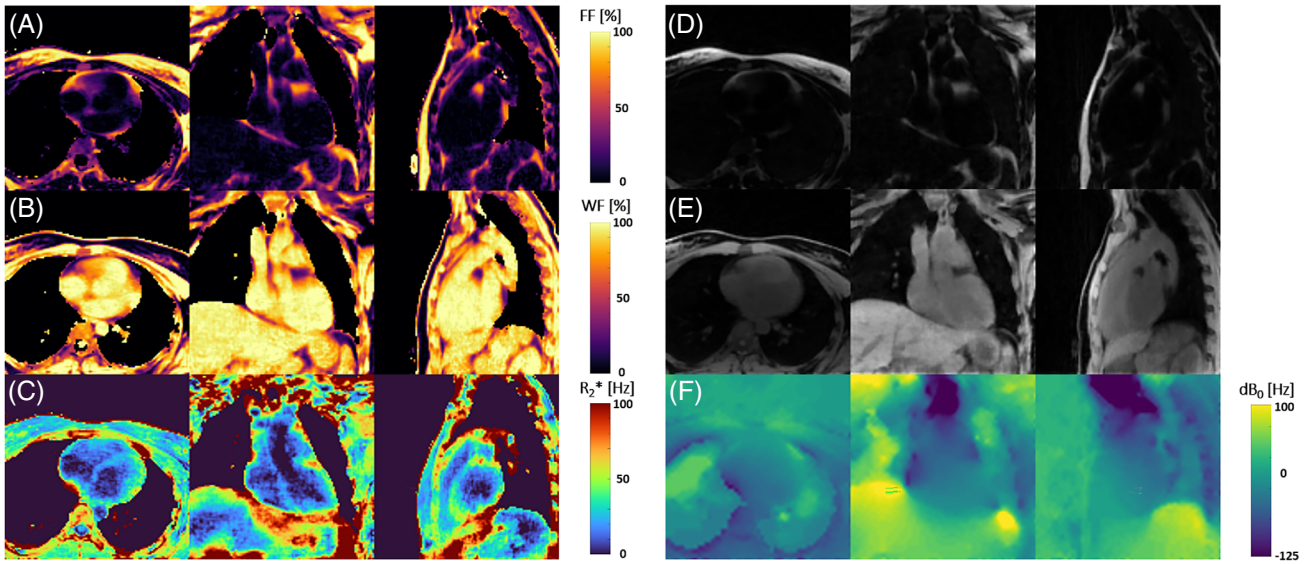

FIGURE 6 Respiratory and cardiac motion-resolved parametric maps in healthy volunteer V3: (A) fat fraction, (B) water fraction, (C) R_2*, and (F) B_0, and separated fat-only (D) and water-only (E) images (see Video S1. for the animation). Transversal, coronal, and sagittal views of the heart at end-expiration are displayed in (A), (B), (D), (E), and (F), whereas (C) displays a different set of slices, selected to highlight the myocardium delineation in the R_2* maps. The animation presented in Video S1 loops through the cardiac cycle.

R_2* values measured in the myocardium were within the expected range for healthy subjects (R_2* < 50 Hz i.e., T_2* > 20 ms). Elevated values (R_2* > 70 Hz) were detected at the interfaces with the liver and the lungs. Compared to the FF and water fraction maps, the R_2* maps displayed a higher SD across the heart, with a more granular aspect, making cardiac motion less visible. The B_0 maps showed good homogeneity in the heart, without variations across the cardiac cycle. Off-resonance deviations were observed outside the heart, with deviations up to 100 Hz seen in the liver. Changes in B_0 across the cardiac bins were only observed within air-filled regions (lungs and FOV periphery).

Measurements in sub-cutaneous fat were not affected by motion binning, with constant FF measured throughout the cardiac cycle in all volunteers (Figure 7A). However, the FF measured in the pericardial fat varied across bins. A consistent pattern was found in all subjects, although to a different extent, with reduced FF at end-systole compared to mid-diastole ($45.7\% \pm 8.3\%$ against $59.1\% \pm 14.9\%$ in V4, $59.0\% \pm 16.5\%$ against $66.0\% \pm 10.0\%$ in V10 after T_1 bias correction). The average decrease in FF observed during end-systole across volunteers was $11.4\% \pm 3.1\%$ after T_1 bias correction. Inspection of the corresponding B_0 maps (Figure 7C) revealed no deviations from one cardiac bin to the next, therefore,

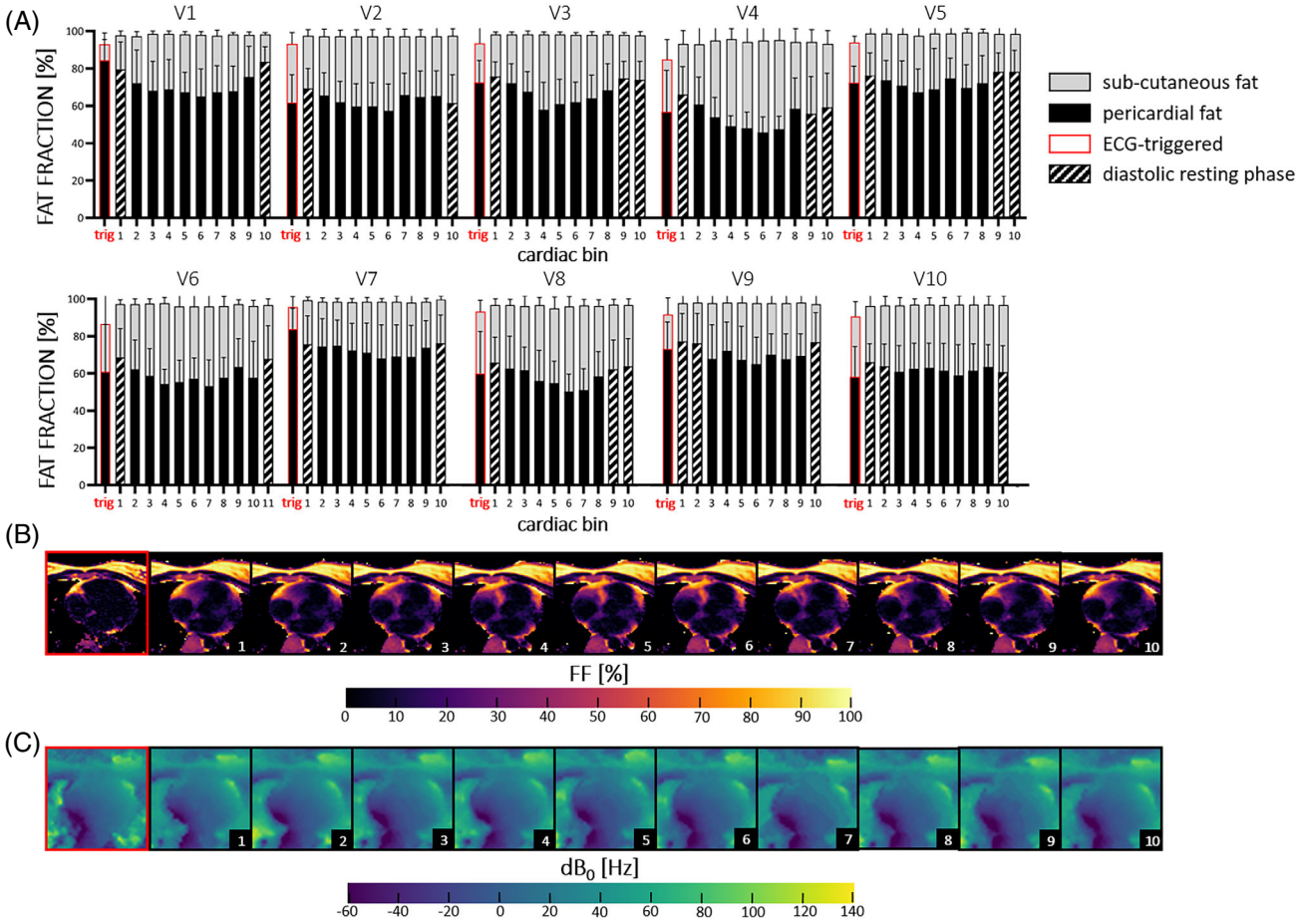

FIGURE 7 Fat quantification throughout the cardiac cycle, after T_1 bias correction. The proposed multiecho gradient echo (ME-GRE) free-running framework allows quantitative visualization and measurement of cardiac fat content at each phase of the cardiac cycle. (A) Average fat fraction and SD measured in regions of interest (ROIs) placed within two tissue types: sub-cutaneous fat and pericardial fat, at expiration. TR-adjusted T_1 bias correction based on T_1 estimates was performed according to the level of bias in the free-running and triggered sequence. In the free-running images, fat fraction was measured in each of the 10 (respectively 11 for volunteer V6) cardiac phases that were re-ordered to place end-diastole at the start (cardiac bin 1). Diastolic resting phase in the free-running images is identified with the white horizontal striped pattern. The matching ROIs reference measurements in electrocardiogram (ECG)-triggered datasets (corresponding to diastolic resting phase) are shown in red borders on the left-hand side of each sub bar plot, with the label "trig." (B) Transversal cardiac fat fraction (FF) maps of healthy volunteer V3, at each cardiac bin as labeled in (A). The displacement of pericardial fatty regions can be followed throughout the cycle. The corresponding slice of the FF map obtained with the 5-echo ECG-triggered protocol is shown on the left, with red borders. (C) Corresponding B_0 maps, which show deviations from the main magnetic field because of system-level imperfections and susceptibility effects. B_0 mapping constitutes an important step of fat quantification techniques with ME-GRE, as the off-resonance caused by the presence of fat has to be decoupled from other sources of off-resonance to be quantified accurately. The corresponding slice of the B_0 map obtained with the 5-echo ECG-triggered protocol is shown on the left, with red borders.

excluding B_0 inhomogeneities as cause of the observed FF variations. Higher SDs were reported in pericardial fat than in sub-cutaneous fat. The average FF measured in the ECG-triggered images was elevated with respect to the free-running diastolic images in six volunteers (Figure 7A). A Bland–Altman analysis showed a bias of −1.06% between the average pericardial FF measured in the free running maps identified as diastolic and the ECG-triggered maps, with 95% limits of agreement at [−8.70;6.58]% (Figure S6). Smaller SDs were observed in the ECG-triggered FF maps. Visually, the ECG triggered FF map had an apparent sharper delineation of the pericardial fatty tissue, where the free-running maps showed fatty regions spread over larger areas (Figure 7B).

Although the free-running FF maps obtained from processing $N_{TE} = 4$ or $N_{TE} = 8$ visually agreed (Figure 8A), significant differences were found in both sub-cutaneous ($p < 0.0001$) and pericardial fat ($p < 0.01$) FF measurements when N_{TE} is reduced (Figure 8C). The influence of a reduced N_{TE} on R_2* quantification was directly discernible from the maps (Figure 8B). Undersampling in the echo dimension resulted in noisy maps, disrupting the

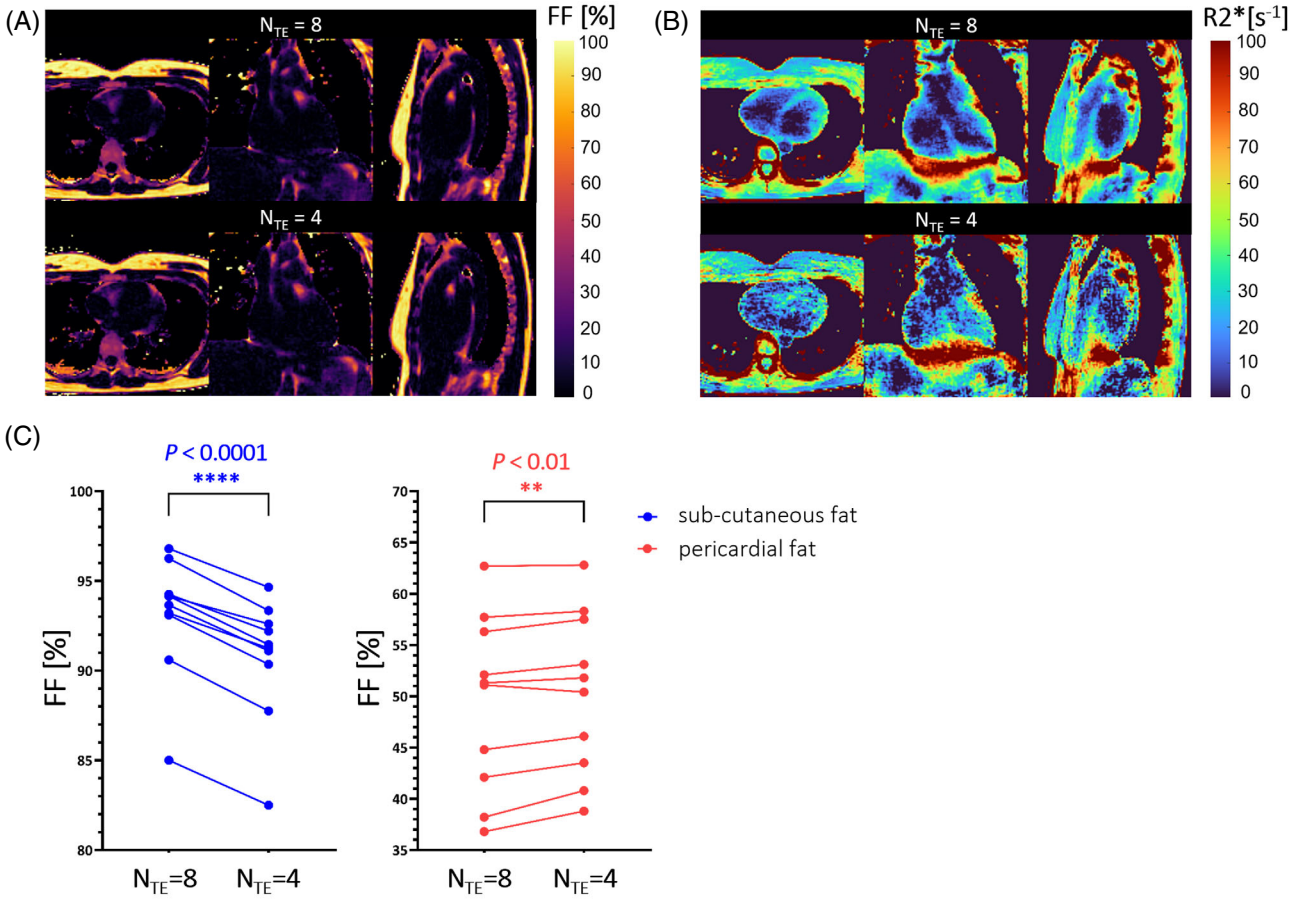

FIGURE 8 Influence of N_{TE} on fat quantification. (A) 3D fat fraction maps obtained with the proposed multiecho gradient echo (ME-GRE) free-running framework, using $N_{TE} = 8$ (top) and $N_{TE} = 4$ (bottom) echoes for chemical species separation and quantification, in volunteer V2. Perfect visual agreement between both sets of images can be observed. (B) 3D R_2* maps obtained with the proposed ME-GRE free-running framework, using $N_{TE} = 8$ (top) and $N_{TE} = 4$ (bottom) echoes in volunteer V2. If a basic delineation of the myocardium muscle is visible in all three orientations with 8 echoes, the undersampled R_2* maps lose this sighting because of high granularity. (C) Average fat fraction in sub-cutaneous and pericardial fat regions of interest (ROIs) measured in 10 selected slices, for all volunteers. The same ROIs were used in both fully sampled and undersampled maps. A paired parametric t-test reveals a highly significant difference ($p < 0.0001$) in sub-cutaneous fat measurements, with a consistent underestimation of the fat content measured with $N_{TE} = 4$ between volunteers. In pericardial fat, the influence of N_{TE} on fat quantification was also detected, but at a lower level of significance ($p < 0.01$).

visualization of anatomy such as myocardium delineation that was present with $N_{TE} = 8$.

4 | DISCUSSION

This study demonstrates the feasibility of free-running whole-heart ME-GRE based fat fraction mapping using retrospective motion resolution based on PT signals and XD-GRASP. The free-running FF mapping approach with PT permits the collection of an unlimited number of echoes, therefore benefiting mapping accuracy. In the current proof-of-concept study, $N_{TE} = 8$ echoes were acquired in a relatively short scan time (6:15 min) for 3D whole-heart coverage, whereas only $N_{TE} = 5$ echoes could be acquired in a corresponding ECG-triggered acquisition with similar TA. With the proposed free-running ME-GRE framework, signal decay as a result of T_2* relaxation provides the only limitation on N_{TE}.

Cardiac motion signals extracted from PT showed an improved correlation with the reference ECG trace than SG signals, confirming previous findings.[50] PT navigation strategies have several advantages compared to SG strategies. First, PT navigation provides a constant and higher sampling frequency (2 kHz). Second, PT signals are insensitive to the underlying trajectory, unlike SG signals, which require a correction for trajectory-dependent signal modulation.[47] Finally, scan time could be further shortened by removing the SI projections. In the current sequence design, the frequency of SI readouts decreases with increasing N_{TE}, therefore affecting temporal resolution: with $N_{TE} = 8$, the SG sampling frequency was 2.67 Hz,

which may hinder cardiac rhythm detection. Although it was not observed to be a limitation in the current healthy volunteer study, it is a potential hurdle for signal extraction in patient populations with abnormal or altered cardiac rhythm. In such cases, PT would remove the need for signal extrapolation, which is otherwise required. Furthermore, the analysis of SG signals extracted from various echoes demonstrated that some frequency components, in particular toward the end of the echo train where SNR is decreased, do not accurately depict cardiac rhythm and therefore, introduce motion blurring. However, despite differences in cardiac signals from the PT and SG sources, the effect on image quality after water–fat separation was minor at $(2\,\text{mm})^3$ spatial resolution. Based on these findings, PT navigation may especially benefit methods where ≥12 echoes are required, such as T_2* or complex fat models. Alternative PT-like methods, such as Beat-PT,[63] have shown promising results for accurate triggering and could be considered to further improve the cardiac signal extraction. Otherwise, SG extraction techniques based on k-space center information could be considered as a way to increase the frequency of motion sampling.[38,41,42,64]

The use of XD-GRASP in this study allowed to recover anatomy that is otherwise barely distinguishable with a simple regridded reconstruction of the heavily undersampled ME-GRE radial data. The reconstruction framework also maintained the contrast changes expected from one echo to another in ME-GRE, and images were in agreement with the reference ECG-triggered ones. Although other free-running studies make use of bSSFP readouts and report strong aliasing because of bright adipose tissue in non-fat suppressed highly accelerated scans,[38] our reconstructed ME-GRE images did not exhibit such artifacts. The current sequence design did not allow for undersampling in the echo dimension, as was done previously,[65] where each subsequent echo had a different trajectory. This approach, as well as rosette-like trajectories[66] where the acquisition of multiple "petals" mimics a multiecho scan, could be exploited to reduce scan time.

The free-running ME-GRE framework enabled quantitative fat measurements across the cardiac cycle, which allows to select a preferred frame for various adipose tissue characterization,[67] and in the current volunteer study, a variable FF pattern was consistently observed as a function of time, indicating an heterogeneity of the pericardial fatty tissue. This result suggests that motion-averaged or frozen-motion (i.e., triggered) visualizations might only allow for partial or incomplete tissue characterization, a finding that can be linked to similar reports on the effect of respiratory motion on R_2* quantification in the liver.[68,69] It remains to be determined whether the observed variation is physiological, or whether ROI drawing on $(2\,\text{mm})^3$ spatial resolution maps might have affected the results. Because no B_0 variations were detected in the heart across the cardiac phases, the observation is not related to B_0 main magnetic field. The B_0 maps produced by the framework mainly serve to separate water and fat, but could have the potential to detect and correct errors or artifacts in images acquired during the same CMR exam that are sensitive to off-resonance.[70] Despite the visual agreement between FF maps obtained with 4 and 8 echoes, significant differences in FF in both static and moving tissues suggest that higher echo sampling benefits mapping accuracy. This is further corroborated by the difference in sub-cutaneous fat FF measurements between the 5-echo ECG-triggered acquisition and the 8-echo free-running acquisition, even after TR-adjusted correction from T_1 bias. If a reduced flip angle approach is commonly used for T_1 bias reduction, phantom results suggest that an a posteriori correction based on T_1 estimates, whereas requiring extra information might be better suited for the proposed framework as it would allow maintaining higher SNR, following the conclusions of Yang et al.[20] T_1 bias could be circumvented with the use of emerging FF quantification methods, which use different ways to encode off-resonance,[71] but are not applicable to ME-GRE data.

Although the same reference fat spectral model was used throughout all the experiments in this study,[57] the sampling of $N_{TE} = 8$ echoes would allow to test different models, including ones with various amounts of peaks (theoretically up to N_{TE}-2 = 6 peaks)[18,23] or ones based on cardiac fatty tissue. Future investigations could, therefore, include the use of self-calibrated spectra, as reported by several studies.[25,72] Although not explored in the current study, the R_2* quantification and the resulting R_2* map suggest that a delineation of the myocardial muscle is possible. The current framework could, therefore, be used for the simultaneous assessment of myocardial iron overload,[73,74] by extending it to bi-exponential relaxation models for a refined estimation.[75,76]

Although the water–fat quantification methods (T_2*-IDEAL, graph cuts algorithm) have been validated thoroughly in phantoms,[24,77] a ground truth measurement for pericardial FF could not be performed in this volunteer study. Besides invasive biopsies and PDFF measured with MRS, which are focal measures, there currently exists no noninvasive reference measurement for whole-heart FF in vivo.

To maintain a reasonable scan time, the data was heavily undersampled and therefore, the binning limited to 10 to 11 cardiac and 2 respiratory phases (Figure S7). Consequently, high regularization was used in the CS reconstruction, allowing to suppress residual sampling artifacts, but at the expense of slightly compressing the motion, as exhibited by the Likert scores in motion resolution (Table S2). This limitation could potentially be

overcome by performing motion compensation in the respiratory domain.[78] Subsequently, this would allow for a cardiac motion-resolved reconstruction with an increased number of cardiac bins[79] and the recovery of a higher Nyquist factor. Furthermore, the addition of motion fields within the reconstruction may provide improved image sharpness and visualization of cardiac fat.[26] The use of a motion-consistent approach based on clustering could also be integrated in this type of golden-angle acquisition.[80]

An additional challenge is the absence of large volumes of fat tissue in our volunteers, which at $(2.0\,\text{mm})^3$ resolution restricts the number of voxels available for quantitative and statistical analysis and makes segmentation more difficult. Future work in patients (displaying wider ranges of FF) would allow for a comparison with invasive biopsies and may help determine whether the proposed framework, at increased spatial resolution, allows for a distinction of epicardial versus pericardial fat, within the frame of coronary artery disease assessment.[81,82]

By incorporating an additional echo dimension within the free-running framework, the present study constitutes a preliminary step toward easier access to whole-heart fat quantification, whereas the presence of cardiac fat as an imaging biomarker undergoes early stage validation.

5 | CONCLUSION

In this study, an MRI framework incorporating a free-running ME-GRE sequence, integrated PT navigation, a robust CS reconstruction, and a multi-peak fat fraction mapping routine was proposed for whole-heart water–fat separation and quantification. The framework combines ease-of-use, robustness to motion, and whole-organ fat quantification without compromising on the number of collected echoes, in a scan time of 6:15 min.

ACKNOWLEDGMENTS

We acknowledge the use of the Fat–Water Toolbox (http://ismrm.org/workshops/FatWater12/data.htm) for some of the results shown in this article. The authors thank Diego Hernando for the valuable discussions and input on this work. This study was supported by funding received from the Swiss National Science Foundation (grants PCEFP2_194296 and PZ00P3_167871 to J.A.M.B., Grant PZ00P3_202140 to C.W.R., grants 320030B_201292 and 320030_173129 to M.S.), the Unil Bourse Pro-Femmes (J.A.M.B.), the Emma Muschamp Foundation (J.A.M.B.) and the Swiss Heart Foundation (grant FF18054 to J.A.M.B.). Open access funding provided by Universitat Bern.

CONFLICT OF INTEREST STATEMENT

Co-authors Mario Bacher, Peter Speier, and Davide Piccini are employees of Siemens Healthcare.

DATA AVAILABILITY STATEMENT

All 10 volunteer datasets, consisting of (1) the free-running and ECG-triggered raw data files; (2) the raw Pilot Tone signals; (3) the extracted respiratory and cardiac signals based on processing of the raw pilot tone signals; and (4) the corresponding time stamps, are publicly available from the following public repositories:

Part 1 (V1–V5): https://zenodo.org/record/7621356#.Y-ZFaXbMLcu.

Part 2 (V6–V10): https://zenodo.org/record/7615780#.Y-ZFfXbMLct.

Volunteer data was collected and approved for open research sharing under the local ethics authorization CER-VD 2021-00708 (Lausanne, Switzerland).

MATLAB scripts to read the raw data, compute the 3D trajectory, and read the raw and extracted pilot tone signals are available from the following public repository: https://github.com/QIS-MRI/ReadDataAndTrajectory_FreeRunningFatFractionHeart.

The compressed-sensing based motion-resolved image reconstruction contains proprietary information that cannot be made available.

ORCID

Christopher W. Roy https://orcid.org/0000-0002-3111-8840

Mariana B. L. Falcão https://orcid.org/0000-0002-4996-0331

Mario Bacher https://orcid.org/0000-0002-5529-3598

Davide Piccini https://orcid.org/0000-0003-4663-3244

Jessica A. M. Bastiaansen https://orcid.org/0000-0002-5485-1308

REFERENCES

1. Reeder SB, Hu HH, Sirlin CB. Proton density fat-fraction: a standardized mr-based biomarker of tissue fat concentration. *J Magn Reson Imaging*. 2012;36:1011-1014. doi:10.1002/jmri.23741
2. Lu M, Zhao S, Jiang S, et al. Fat deposition in dilated cardiomyopathy assessed by CMR. *JACC Cardiovasc Imaging*. 2013;6:889-898. doi:10.1016/j.jcmg.2013.04.010
3. Burke AP, Farb A, Tashko G, Virmani R. Arrhythmogenic right ventricular cardiomyopathy and fatty replacement of the right ventricular myocardium. *Circulation*. 1998;97:1571-1580. doi:10.1161/01.CIR.97.16.1571
4. Kellman P, Hernando D, Shah S, et al. Multiecho Dixon fat and water separation method for detecting fibrofatty infiltration in the myocardium. *Magn Reson Med*. 2009;61:215-221. doi:10.1002/mrm.21657
5. Mordi I, Radjenovic A, Stanton T, et al. Prevalence and prognostic significance of Lipomatous metaplasia in patients

with prior myocardial infarction. *JACC Cardiovasc Imaging*. 2015;8:1111-1112. doi:10.1016/j.jcmg.2014.07.024
6. Baroldi G, Silver MD, De Maria R, Parodi O, Pellegrini A. Lipomatous metaplasia in left ventricular scar. *Can J Cardiol*. 1997;13:65-71.
7. Gorter PM, van Lindert ASR, de Vos AM, et al. Quantification of epicardial and peri-coronary fat using cardiac computed tomography; reproducibility and relation with obesity and metabolic syndrome in patients suspected of coronary artery disease. *Atherosclerosis*. 2008;197:896-903. doi:10.1016/j.atherosclerosis.2007.08.016
8. Franz D, Weidlich D, Freitag F, et al. Association of proton density fat fraction in adipose tissue with imaging-based and anthropometric obesity markers in adults. *Int J Obes (Lond)*. 2018;42:175-182. doi:10.1038/ijo.2017.194
9. Rosito GA, Massaro JM, Hoffmann U, et al. Pericardial fat, visceral abdominal fat, cardiovascular disease risk factors, and vascular calcification in a community-based sample. *Circulation*. 2008;117:605-613. doi:10.1161/CIRCULATIONAHA.107.743062
10. Cordes C, Baum T, Dieckmeyer M, et al. MR-based assessment of bone marrow fat in osteoporosis, diabetes, and obesity. *Front Endocrinol*. 2016;7:74. doi:10.3389/fendo.2016.00074
11. Sironi AM, Petz R, De Marchi D, et al. Impact of increased visceral and cardiac fat on cardiometabolic risk and disease: visceral, epicardial and/or intrathoracic fat? *Diabet Med*. 2012;29:622-627. doi:10.1111/j.1464-5491.2011.03503.x
12. Chen O, Sharma A, Ahmad I, et al. Correlation between pericardial, mediastinal, and intrathoracic fat volumes with the presence and severity of coronary artery disease, metabolic syndrome, and cardiac risk factors. *Eur Heart J – Cardiovasc Imaging*. 2015;16:37-46. doi:10.1093/ehjci/jeu145
13. Reeder SB, Wen Z, Yu H, et al. Multicoil Dixon chemical species separation with an iterative least-squares estimation method. *Magn Reson Med*. 2004;51:35-45. doi:10.1002/mrm.10675
14. Bray TJ, Chouhan MD, Punwani S, Bainbridge A, Hall-Craggs MA. Fat fraction mapping using magnetic resonance imaging: insight into pathophysiology. *Br J Radiol*. 2018;91:20170344. doi:10.1259/bjr.20170344
15. Yu H, Reeder SB, Shimakawa A, Brittain JH, Pelc NJ. Field map estimation with a region growing scheme for iterative 3-point water-fat decomposition. *Magn Reson Med*. 2005;54:1032-1039. doi:10.1002/mrm.20654
16. Tsao J, Jiang Y. Hierarchical IDEAL: fast, robust, and multiresolution separation of multiple chemical species from multiple echo times. *Magn Reson Med*. 2013;70:155-159. doi:10.1002/mrm.24441
17. Lu W, Hargreaves BA. Multiresolution field map estimation using golden section search for water-fat separation. *Magn Reson Med*. 2008;60:236-244. doi:10.1002/mrm.21544
18. Hernando D, Kellman P, Haldar JP, Liang Z-P. Robust water/fat separation in the presence of large field inhomogeneities using a graph cut algorithm. *Magn Reson Med*. 2009;63:7990. doi:10.1002/mrm.22177
19. Bydder M, Yokoo T, Hamilton G, et al. Relaxation effects in the quantification of fat using gradient echo imaging. *Magn Reson Imaging*. 2008;26:347-359. doi:10.1016/j.mri.2007.08.012
20. Yang IY, Cui Y, Wiens CN, Wade TP, Friesen-Waldner LJ, McKenzie CA. Fat fraction bias correction using T1 estimates and flip angle mapping. *J Magn Reson Imaging*. 2014;39:217-223. doi:10.1002/jmri.24126
21. Yu H, McKenzie CA, Shimakawa A, et al. Multiecho reconstruction for simultaneous water-fat decomposition and T2* estimation. *J Magn Reson Imaging*. 2007;26:1153-1161. doi:10.1002/jmri.21090
22. Liu C-Y, McKenzie CA, Yu H, Brittain JH, Reeder SB. Fat quantification with IDEAL gradient echo imaging: correction of bias from T1 and noise. *Magn Reson Med*. 2007;58:354-364. doi:10.1002/mrm.21301
23. Yu H, Shimakawa A, McKenzie CA, Brodsky E, Brittain JH, Reeder SB. Multiecho water-fat separation and simultaneous R estimation with multifrequency fat spectrum modeling. *Magn Reson Med*. 2008;60:1122-1134. doi:10.1002/mrm.21737
24. Hines CDG, Yu H, Shimakawa A, McKenzie CA, Brittain JH, Reeder SB. T1 independent, T2* corrected MRI with accurate spectral modeling for quantification of fat: validation in a fat-water-SPIO phantom. *J Magn Reson Imaging*. 2009;30:1215-1222. doi:10.1002/jmri.21957
25. Kühn J-P, Hernando D, Muñoz del Rio A, et al. Effect of multipeak spectral modeling of fat for liver iron and fat quantification: correlation of biopsy with MR imaging results. *Radiology*. 2012;265:133-142. doi:10.1148/radiol.12112520
26. Mayer J, Blaszczyk E, Cipriani A, et al. Cardio-respiratory motion-corrected 3D cardiac water-fat MRI using model-based image reconstruction. *Magn Reson Med*. 2022;88:1561-1574. doi:10.1002/mrm.29284
27. Liu J, Nguyen TD, Zhu Y, et al. Self-gated free-breathing 3D coronary CINE imaging with simultaneous water and fat visualization. *PLOS One*. 2014;9:e89315. doi:10.1371/journal.pone.0089315
28. Taviani V, Hernando D, Francois CJ, et al. Whole-heart chemical shift encoded water–fat MRI. *Magn Reson Med*. 2014;72:718-725. doi:10.1002/mrm.24982
29. Munoz C, Cruz G, Neji R, Botnar RM, Prieto C. Motion corrected water/fat whole-heart coronary MR angiography with 100% respiratory efficiency. *Magn Reson Med*. 2019;82:732-742. doi:10.1002/mrm.27732
30. Dietrich S, Aigner CS, Mayer J, et al. Motion-compensated fat-water imaging for 3D cardiac MRI at ultra-high fields. *Magn Reson Med*. 2022;87:2621-2636. doi:10.1002/mrm.29144
31. Jaubert O, Cruz G, Bustin A, et al. Water–fat Dixon cardiac magnetic resonance fingerprinting. *Magn Reson Med*. 2020;83:2107-2123. doi:10.1002/mrm.28070
32. Jaubert O, Cruz G, Bustin A, et al. T1, T2, and fat fraction cardiac MR fingerprinting: preliminary clinical evaluation. *J Magn Reson Imaging*. 2021;53:1253-1265. doi:10.1002/jmri.27415
33. Lima da Cruz GJ, Velasco C, Lavin B, Jaubert O, Botnar RM, Prieto C. Myocardial T1, T2, T2*, and fat fraction quantification via low-rank motion-corrected cardiac MR fingerprinting. *Magn Reson Med*. 2022;87:2757-2774. doi:10.1002/mrm.29171
34. Goldfarb JW, Craft J, Cao JJ. Water–fat separation and parameter mapping in cardiac MRI via deep learning with a convolutional neural network. *J Magn Reson Imaging*. 2019;50:655-665. doi:10.1002/jmri.26658
35. Coppo S, Piccini D, Bonanno G, et al. Free-running 4D whole-heart self-navigated golden angle MRI: initial results. *Magn Reson Med*. 2015;74:1306-1316. doi:10.1002/mrm.25523
36. Bastiaansen JAM, Piccini D, Di Sopra L, et al. Natively fat-suppressed 5D whole-heart MRI with a radial free-running

fast-interrupted steady-state (FISS) sequence at 1.5T and 3T. *Magn Reson Med*. 2020;83:45-55. doi:10.1002/mrm.27942

37. Franceschiello B, Di Sopra L, Minier A, et al. 3-dimensional magnetic resonance imaging of the freely moving human eye. *Prog Neurobiol*. 2020;194:101885. doi:10.1016/j.pneurobio.2020.101885
38. Küstner T, Bustin A, Jaubert O, et al. Fully self-gated free-running 3D Cartesian cardiac CINE with isotropic whole-heart coverage in less than 2 min. *NMR Biomed*. 2021;34:e4409. doi:10.1002/nbm.4409
39. Masala N, Bastiaansen JAM, Sopra LD, et al. Free-running 5D coronary MR angiography at 1.5T using LIBRE water excitation pulses. *Magn Reson Med*. 2020;84:1470-1485. doi:10.1002/mrm.28221
40. Ishida M, Yerly J, Ito H, et al. Optimal protocol for contrast-enhanced free-running 5D whole-heart coronary MR angiography at 3T. *Magn Reson Med Sci*. 2023;0086. doi:10.2463/mrms.tn.2022-0086
41. Qi H, Bustin A, Cruz G, et al. Free-running simultaneous myocardial T1/T2 mapping and cine imaging with 3D whole-heart coverage and isotropic spatial resolution. *Magn Reson Imaging*. 2019;63:159-169. doi:10.1016/j.mri.2019.08.008
42. Qi H, Jaubert O, Bustin A, et al. Free-running 3D whole heart myocardial T1 mapping with isotropic spatial resolution. *Magn Reson Med*. 2019;82:1331-1342. doi:10.1002/mrm.27811
43. Shaw JL, Yang Q, Zhou Z, et al. Free-breathing, non-ECG, continuous myocardial T1 mapping with cardiovascular magnetic resonance multitasking. *Magn Reson Med*. 2019;81:2450-2463. doi:10.1002/mrm.27574
44. Christodoulou AG, Shaw JL, Nguyen C, et al. Magnetic resonance multitasking for motion-resolved quantitative cardiovascular imaging. *Nat Biomed Eng*. 2018;2:215-226. doi:10.1038/s41551-018-0217-y
45. Ma LE, Yerly J, Piccini D, et al. 5D flow MRI: a fully self-gated, free-running framework for cardiac and respiratory motion–resolved 3D hemodynamics. *Radiol Cardiothorac Imaging*. 2020;2:e200219. doi:10.1148/ryct.2020200219
46. Feng L, Coppo S, Piccini D, et al. 5D whole-heart sparse MRI. *Magn Reson Med*. 2018;79:826-838. doi:10.1002/mrm.26745
47. Di Sopra L, Piccini D, Coppo S, Stuber M, Yerly J. An automated approach to fully self-gated free-running cardiac and respiratory motion-resolved 5D whole-heart MRI. *Magn Reson Med*. 2019;82:2118-2132. doi:10.1002/mrm.27898
48. Speier P. PT-Nav: a novel respiratory navigation method for continuous acquisitions based on modulation of a pilot tone in the MR-receiver. *Proc ESMRMB*. 2015;129:97-98.
49. Vahle T, Bacher M, Rigie D, et al. Respiratory motion detection and correction for MR using the pilot tone: applications for MR and simultaneous PET/MR exams. *Invest Radiol*. 2020;55:153-159. doi:10.1097/RLI.0000000000000619
50. Falcão MBL, Di Sopra L, Ma L, et al. Pilot tone navigation for respiratory and cardiac motion-resolved free-running 5D flow MRI. *Magn Reson Med*. 2022;87:718-732. doi:10.1002/mrm.29023
51. Piccini D, Littmann A, Nielles-Vallespin S, Zenge MO. Spiral phyllotaxis: the natural way to construct a 3D radial trajectory in MRI. *Magn Reson Med*. 2011;66:1049-1056. doi:10.1002/mrm.22898
52. Bush EC, Gifford A, Coolbaugh CL, Towse TF, Damon BM, Welch EB. Fat-water phantoms for magnetic resonance imaging validation: a flexible and scalable protocol. *Jove J Vis Exp*. 2018;139:57704. doi:10.3791/57704
53. Zhong X, Hu HH, Armstrong T, et al. Free-breathing volumetric liver and proton density fat fraction quantification in pediatric patients using stack-of-radial MRI with self-gating motion compensation. *J Magn Reson Imaging*. 2021;53:118-129. doi:10.1002/jmri.27205
54. Feng L, Axel L, Chandarana H, Block KT, Sodickson DK, Otazo R. XD-GRASP: Golden-angle radial MRI with reconstruction of extra motion-state dimensions using compressed sensing. *Magn Reson Med*. 2016;75:775-788. doi:10.1002/mrm.25665
55. Boyd S, Parikh N, Chu E, Peleato B, Eckstein J. Distributed optimization and statistical learning via the alternating direction method of multipliers. *Found Trends® Mach Learn*. 2011;3:1-122. doi:10.1561/2200000016
56. Boykov Y, Veksler O, Zabih R. Fast approximate energy minimization via graph cuts. *IEEE Trans Pattern Anal Mach Intell*. 2001;23:1222-1239. doi:10.1109/34.969114
57. Hu HH, Börnert P, Hernando D, et al. ISMRM workshop on fat–water separation: insights, applications and progress in MRI. *Magn Reson Med*. 2012;68:378-388. doi:10.1002/mrm.24369
58. Pang J, Sharif B, Fan Z, et al. ECG and navigator-free four-dimensional whole-heart coronary MRA for simultaneous visualization of cardiac anatomy and function. *Magn Reson Med*. 2014;72:1208-1217. doi:10.1002/mrm.25450
59. Hamilton JI, Pahwa S, Adedigba J, et al. Simultaneous mapping of T1 and T2 using cardiac magnetic resonance fingerprinting in a cohort of healthy subjects at 1.5T. *J Magn Reson Imaging*. 2020;52:1044-1052. doi:10.1002/jmri.27155
60. de Bazelaire CMJ, Duhamel GD, Rofsky NM, Alsop DC. MR imaging relaxation times of abdominal and pelvic tissues measured in vivo at 3.0 T: preliminary results. *Radiology*. 2004;230:652-659. doi:10.1148/radiol.2303021331
61. Taylor AJ, Salerno M, Dharmakumar R, Jerosch-Herold M. T1 mapping: basic techniques and clinical applications. *JACC Cardiovasc Imaging*. 2016;9:67-81. doi:10.1016/j.jcmg.2015.11.005
62. Cao T, Wang N, Kwan AC, et al. Free-breathing, non-ECG, simultaneous myocardial T1, T2, T2*, and fat-fraction mapping with motion-resolved cardiovascular MR multitasking. *Magn Reson Med*. 2022;88:1748-1763. doi:10.1002/mrm.29351
63. Anand S, Lustig M. Beat pilot tone: exploiting preamplifier intermodulation of UHF/SHF RF for improved motion sensitivity over pilot tone navigators. *Proc Intl Soc Mag Reson Med*. 2021;29:0568.
64. Liu J, Spincemaille P, Codella NCF, Nguyen TD, Prince MR, Wang Y. Respiratory and cardiac self-gated free-breathing cardiac CINE imaging with multiecho 3D hybrid radial SSFP acquisition. *Magn Reson Med*. 2010;63:1230-1237. doi:10.1002/mrm.22306
65. Benkert T, Feng L, Sodickson DK, Chandarana H, Block KT. Free-breathing volumetric fat/water separation by combining radial sampling, compressed sensing, and parallel imaging. *Magn Reson Med*. 2017;78:565-576. doi:10.1002/mrm.26392
66. Liu Y, Hamilton J, Eck B, Griswold M, Seiberlich N. Myocardial T1 and T2 quantification and water–fat separation using cardiac MR fingerprinting with rosette trajectories at 3T and 1.5T. *Magn Reson Med*. 2021;85:103-119. doi:10.1002/mrm.28404
67. Daudé P, Ancel P, Confort Gouny S, et al. Deep-learning segmentation of Epicardial adipose tissue using four-chamber

cardiac magnetic resonance imaging. *Diagnostics*. 2022;12:126. doi:10.3390/diagnostics12010126
68. Zhong X, Armstrong T, Nickel MD, et al. Effect of respiratory motion on free-breathing 3D stack-of-radial liver relaxometry and improved quantification accuracy using self-gating. *Magn Reson Med*. 2020;83:1964-1978. doi:10.1002/mrm.28052
69. Schneider M, Benkert T, Solomon E, et al. Free-breathing fat and R2* quantification in the liver using a stack-of-stars multi-echo acquisition with respiratory-resolved model-based reconstruction. *Magn Reson Med*. 2020;84:2592-2605. doi:10.1002/mrm.28280
70. Kellman P, Herzka DA, Arai AE, Hansen MS. Influence of off-resonance in myocardial T1-mapping using SSFP based MOLLI method. *J Cardiovasc Magn Reson*. 2013;15:63. doi:10.1186/1532-429X-15-63
71. Rossi GM, Hilbert T, Mackowiak AL, Pierzchała K, Kober T, Bastiaansen JA. Fat fraction mapping using bSSFP signal profile asymmetries for robust multi-compartment quantification (SPARCQ). 2020. doi:10.48550/arXiv.2005.09734
72. Reeder SB, Robson PM, Yu H, et al. Quantification of hepatic steatosis with MRI: the effects of accurate fat spectral modeling. *J Magn Reson Imaging*. 2009;29:1332-1339. doi:10.1002/jmri.21751
73. Triadyaksa P, Oudkerk M, Sijens PE. Cardiac T2* mapping: techniques and clinical applications. *J Magn Reson Imaging*. 2020;52:1340-1351. doi:10.1002/jmri.27023
74. Mavrogeni S. Evaluation of myocardial iron overload using magnetic resonance imaging. *Blood Transfus*. 2009;7:183-187. doi:10.2450/2008.0063-08
75. Juras V, Apprich S, Zbýň Š, et al. Quantitative MRI analysis of menisci using biexponential T2* fitting with a variable echo time sequence. *Magn Reson Med*. 2014;71:1015-1023. doi:10.1002/mrm.24760
76. Positano V, Salani B, Pepe A, et al. Improved T2* assessment in liver iron overload by magnetic resonance imaging. *Magn Reson Imaging*. 2009;27:188-197. doi:10.1016/j.mri.2008.06.004
77. Hernando D, Sharma SD, Aliyari Ghasabeh M, et al. Multisite, multivendor validation of the accuracy and reproducibility of proton-density fat-fraction quantification at 1.5T and 3T using a fat–water phantom. *Magn Reson Med*. 2017;77:1516-1524. doi:10.1002/mrm.26228
78. Roy CW, Heerfordt J, Piccini D, et al. Motion compensated whole-heart coronary cardiovascular magnetic resonance angiography using focused navigation (fNAV). *J Cardiovasc Magn Reson*. 2021;23:33. doi:10.1186/s12968-021-00717-4
79. Falcão MBL, Rossi GM, Ma LE, et al. Correcting versus resolving respiratory motion in accelerated free-running whole-heart radial flow MRI using focused navigation (fNAV). *Proc Intl Soc Mag Reson Med*. 2021;29:0304.
80. Heerfordt J, Whitehead KK, Bastiaansen JAM, et al. Similarity-driven multi-dimensional binning algorithm (SIMBA) for free-running motion-suppressed whole-heart MRA. *Magn Reson Med*. 2021;86:213-229. doi:10.1002/mrm.28713
81. Ahn S-G, Lim H-S, Joe D-Y, et al. Relationship of epicardial adipose tissue by echocardiography to coronary artery disease. *Heart*. 2008;94:e7–e7. doi:10.1136/hrt.2007.118471
82. Guglielmo M, Lin A, Dey D, et al. Epicardial fat and coronary artery disease: role of cardiac imaging. *Atherosclerosis*. 2021;321:30-38. doi:10.1016/j.atherosclerosis.2021.02.008

SUPPORTING INFORMATION

Additional supporting information may be found in the online version of the article at the publisher's website.

Table S1. Heart rate detection limitations.
Table S2. Blinded scoring according to a 5-point Likert scale, averaged over $n = 10$ volunteers.
Figure S1. Comparison to Cartesian sampling trajectory in a phantom with controlled fat fraction vials.
Figure S2. 3D radial phyllotaxis trajectories.
Figure S3. Motion-resolved image reconstruction with XD-GRASP.
Figure S4. Filtering trajectory-dependent frequency components from self-gating signals.
Figure S5. Linear regression of pilot tone versus ECG mean estimated cardiac cycle length in 10 volunteers.
Figure S6. Bland–Altman (a) and regression (b) analysis of fat content measured in free-running images identified as diastolic resting phase, versus ECG-triggered data, after T_1 bias correction.
Table S3. Peak-to-peak respiratory amplitudes.
Figure S7. Respiratory curves and binning in two volunteers.

Video S1. Proof-of-concept respiratory and cardiac motion-resolved parametric maps in healthy volunteer V3: (a) fat fraction, (b) water fraction, (c) R_2* and (d) B_0, and separated fat-only (e) and water-only (f) images.

How to cite this article: Mackowiak ALC, Roy CW, Yerly J, et al. Motion-resolved fat-fraction mapping with whole-heart free-running multiecho GRE and pilot tone. *Magn Reson Med*. 2023;1-17. doi: 10.1002/mrm.29680